Contents lists available at ScienceDirect

Applied Catalysis B: Environmental

Extraordinary sensitizing effect of co-doped carbon nanodots derived from mate herb: Application to enhanced photocatalytic degradation of chlorinated wastewater compounds under visible light

M. Carmen Ortega-Liebana [a,b], Jose L. Hueso [a,b,*], Shammi Ferdousi [c], Raul Arenal [d,e], Silvia Irusta [a,b], King L. Yeung [c], Jesus Santamaria [a,b,*]

[a] Institute of Nanoscience of Aragon (INA) and Department of Chemical Engineering and Environmental Technology, University of Zaragoza, 50018, Zaragoza, Spain
[b] Networking Research Center on Bioengineering, Biomaterials and Nanomedicine (CIBER-BBN), 28029 Madrid, Spain
[c] Department of Chemical and Biomolecular Engineering, The Hong Kong University of Science and Technology (HKUST), Clear Water Bay, Kowloon, Hong Kong, China
[d] Laboratorio de Microscopías Avanzadas, Instituto de Nanociencia de Aragón, Universidad de Zaragoza, 50018 Zaragoza, Spain
[e] ARAID Foundation, 50018 Zaragoza, Spain

ARTICLE INFO

ABSTRACT

The present work investigates the role of two types of carbon nanodots (CNDs) as novel sensitizers of TiO_2 to create a visible-light driven photo-catalyst that is not only efficient for solar-driven pollution abatement, but also inexpensive, durable and environmentally-friendly. Two widely available green organic precursors, the Argentinean herb Mate and the Stevia plant have been selected as the carbogenic source to thermally induce the formation of different types of CNDs with different levels of N and P doping and tunable photoluminescence response in the UV–vis-near infrared (NIR) ranges. These CNDs have been successfully assembled with TiO_2 to form heterogeneous photocatalysts that are highly active in the visible-light and NIR- driven photodegradation of 2,4-dichlorophenol (2,4-DCP), a persistent chlorinated organic compound present in numerous pesticide formulations.

© 2017 Elsevier B.V. All rights reserved.

1. Introduction

The growing volume of wastes generated by human activities represents one of the most urgent environmental challenges that we face today [1–4]. Persistent and non-biodegradable organics in wastewater are major problems in water management, environmental protection, and water reuse. Traditional treatment methods such as adsorption, coagulation, and secondary biodegradation are often inadequate in treating many of the new, emerging micro-pollutants. They also suffer from high capital and operating costs, and are known to generate undesired secondary pollutants. Advanced oxidation processes (AOPs) [4–9] are capable of efficiently treating a broad range of problematic and refractory organic pollutants in water. The highly reactive radical species and oxidative intermediates (i.e. H_2O_2, $^\bullet OH$, $^\bullet O_2^-$, O_3) provide more complete oxidation and mineralization of the pollutants. Heterogeneous photocatalysis is particularly attractive for wastewater treatment with a clear advantage in terms of cost when the process is solar driven [1,5,8,10–12].

Current research is focused mainly on the optimization of the state-of-the-art solid heterogeneous photocatalysts. These materials are typically semiconductors that can be susceptible to photo-corrosion during long-term operation. Titania photocatalysts are remarkably stable under varied operating conditions and due to their abundance are less expensive than alternative materials [2,3,8]. Nevertheless, TiO_2 having a wide electronic band-gap requires UV irradiation. Moreover, rapid recombination of

* Corresponding authors at: Institute of Nanoscience of Aragon (INA) and Department of Chemical Engineering and Environmental Technology, University of Zaragoza, 50018, Zaragoza, Spain.
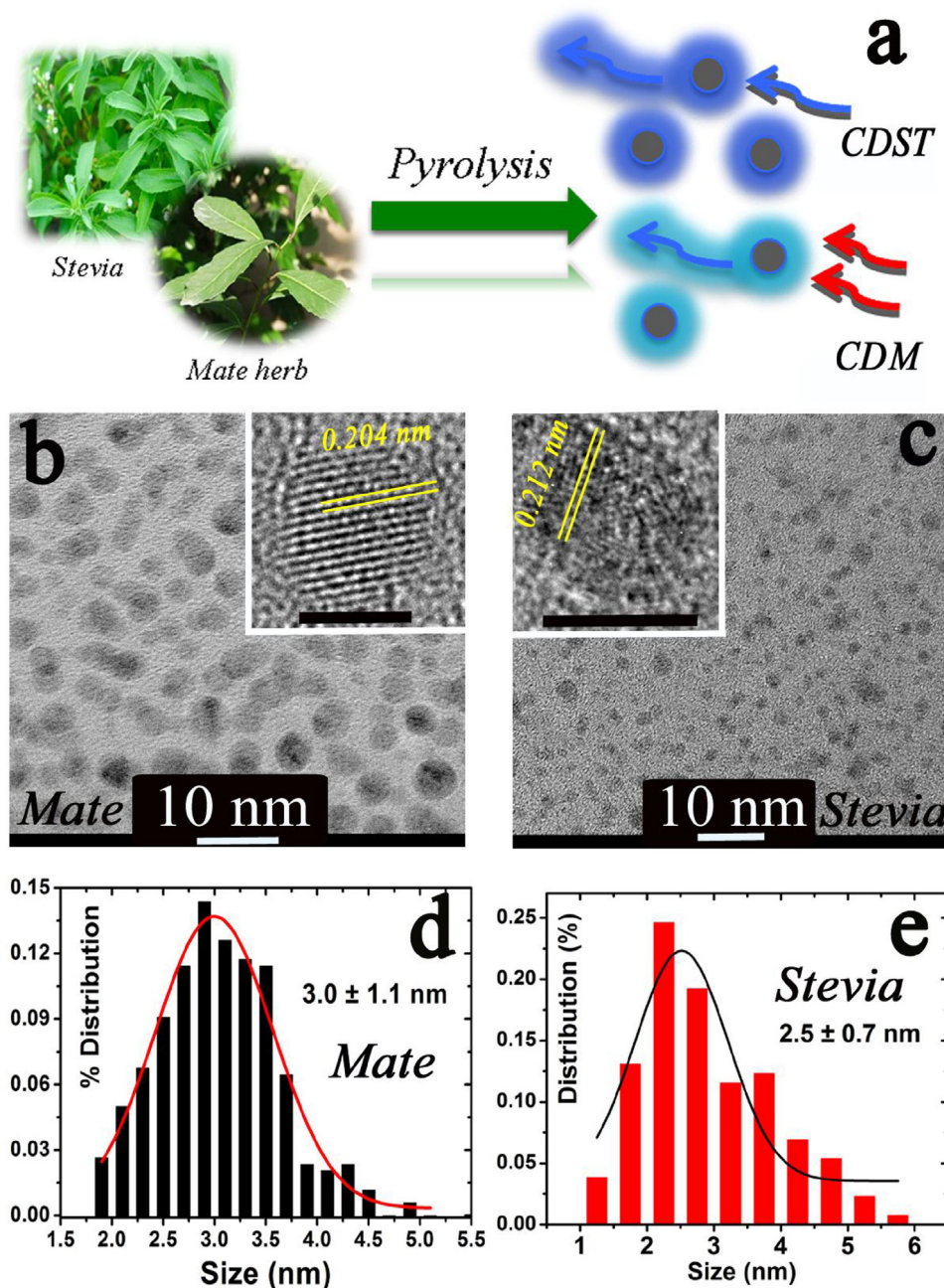E-mail addresses: jlhueso@unizar.es (J.L. Hueso), jesus.santamaria@unizar.es (J. Santamaria).

Fig. 1. (a) Scheme of the pyrolysis treatment of Mate and Stevia plant leaves; (b) TEM image of the carbon nanodots retrieved from Mate (inset: HRTEM image of a single CND with (111) orientation corresponding to graphite); (c) TEM image corresponding to the carbon nanodots obtained from the Stevia plant (inset: HRTEM image of a single CND where lattice distances for (020) orientations of graphite are shown); (d) Particle size distribution of the CNDM; (e) Particle size distribution of the CNDST. Scale bars in insets correspond to 3 nm.

the photo-generated electron-hole pair can significantly limit the quantum efficiency. Therefore, narrowing down the band-gap of TiO_2 to increase the visible-light absorption response is an often-used strategy to improve the photocatalyst performance [13,14]. Among the procedures employed are: (i) chemical modifications with light elements such as carbon, nitrogen, boron or sulfur to shift the absorption toward the visible range by creating intermediate energy states that narrow the band gap [13,14]; (ii) addition of plasmonic noble metals that boost absorption in the visible-NIR range due to their surface plasmon resonance (SPR) band [15–21]; (iii) use of sensitizers such as organic dyes and/or narrow band-gap quantum dots that absorb visible light and inject electrons into the conduction band of TiO_2 to suppress the recombination rate of

electron-hole pairs as in the case of quantum dot sensitized solar cells (QDSSCs) [22–25].

This work investigates the use of carbon nanodots (CNDs) in TiO_2 to create a visible-light photo-catalyst that not only is efficient for solar-driven pollution abatement, but also inexpensive, durable and environmentally-friendly [26–34]. Carbon nanodots are luminescent nanomaterials characterized by their broad absorption spectra, resistance to photo-bleaching and low toxicity [30,31,33–39]. They are potentially inexhaustible in view of the abundance of raw materials for their production. CNDs may also exhibit an interesting optical behavior as up-converters, thanks to due to size-dependent quantum confinement effects, expanding their potential applicability as sensitizers in the whole solar

spectrum [27,33,40–47]. Plant leaves and extracts abound with carbon, nitrogen and oxygen elements [47] which may serve as easily available carbon sources for large-scale fabrication of CNDs.

Herein, the preparation of new carbon dots from renewable plant materials has been successfully explored with two low-cost, widely available raw materials: the *Mate* herb (*Ilex paraguariensis*) and the stevia plant (*Stevia rebaudiana*). We have observed that the carbon dots obtained from the different plant sources exhibited unique sensitizing capabilities associated with the specific chemical compositions of the precursors. Furthermore, different levels of doping with nitrogen and phosphor can be achieved depending on the starting plant leaf and it is possible to tailor the resulting green carbon nanodots with different optical response as up-converters or down-converters. Finally, we have easily prepared photocatalytic nanohybrids by self-assembly of our N,P co-doped carbon nanodots onto commercial TiO_2 heterogeneous photocatalysts and used them towards the visible-light driven photodegradation of 2,4-dichlorophenol, a persistent chlorinated organic compound present in numerous pesticide formulations.

2. Experimental

2.1. Materials and reagents

Titanium (IV) dioxide (anatase, 99.8%) terephtalic acid (TA, 98%) and 2,4-dichlorophenol (99%) were purchased from Aldrich. Ethylenediaminetetraacetic acid disodium salt (ACS reagent, 99–101%, EDTA-Na_2), 1-butanol (ACS reagent grade) and quinine hemisulphate salt monohydrate (Bioreagent, 98%) were purchased and used without any further purification steps. The mate herb (*Ilex paraguariensis*) was supplied by Cruz Malta and the stevia leaves (*Stevia rebaudiana*) were purchased from Herbalism. Ultrapure water from a Milli-Q ultrapure system was used in this study.

2.2. Synthesis of carbon nanoparticles

CNDs were prepared by pyrolysis of plant leaves (Fig. 1a). The mate herb and the stevia leaves were first dried in an oven at 100 °C prior to grinding into a fine powder. 1.2 g of the dried and powdered mate and stevia leaves were thermally treated in still air for 2 h at 300 °C and 250 °C, respectively. Black carbonized powder was cooled to room temperature, dispersed in ultrapure water (i.e., 15 mL) and centrifuged at 6000 rpm for 10 min to remove large or agglomerated particles. The remaining supernatant was filtered through a 0.1 μm PTFE membrane (WhatmanTH) to give a brownish yellow suspension of CNDs. No presence of additional agglomerates was detected in the final suspension. The CNDs from mate and stevia leaves were named as CNDM and CNDST, respectively. It was observed that other heating temperatures did not render CNDs as indicated by a large decrease in the photoluminescence (PL) intensities and the absence of a representative population of CNDs. According to the literature 250–300 °C is enough for the preparation of CNDs [48].

2.3. Synthesis of CNDs/TiO$_2$ nanohybrids

CND/TiO$_2$ composites were synthesized by a simple room-temperature process. 0.5 g Anatase TiO$_2$ powders were first dispersed in a mixture of 2.6 mL CNDs solution (1 mg/mL) and 2.4 mL deionized water, and stirred vigorously for 30 min. The resulting suspension was dried under vacuum at 65 °C for 90 min and stored at ambient conditions until further use. The syntheses were performed using the facilities of the NANBIOSIS ICTS, more specifically by the Nanoparticle Synthesis Unit of the CIBER in Bio-Engineering, Biomaterials & Nanomedicine (CIBER-BBN).

2.4. Photocatalytic activity

The photocatalytic activity of the nanohybrids was evaluated by degradation of 2,4-DCP under visible light or under specific near-infrared (NIR) irradiation. A Hg lamp (blanklight blue F6T5BLB, with a cutoff filter λ < 420 nm) for visible light and a light-emitting diode (LED ENGIN, LZ4 model) at 740 nm for NIR experiments, respectively. 20 mg nanohybrids were suspended in 100 mL, 0.025 mM 2,4-DCP aqueous solution and stirred for 12–20 h to approach adsorption equilibrium between 2,4-DCP and photocatalyst before irradiation. Under stirring, a small amount of the suspension (about 3 mL) was taken at different times under irradiation and filtered through a 0.22 μm filter. The liquid was analyzed using an ultra performance liquid chromatography (UPLC) or GC–MS.

2.5. Detection of reactive oxidative species (ROS) generated by NIR illumination

The generation of hydroxyl radical under NIR irradiation was evaluated using terephtalic acid (TA) as a probe, which selectively reacts with ·OH to form a fluorescent derivative [30,49]. In a typical procedure, the detection of hydroxyl radicals (·OH) was carried out with the aid of terephthalic acid (TA, 3 mL, 5 mM) which selectively reacts to generate a fluorescent product (2-hydroxy terephthalic acid) emitting at ca. 425 nm. It is important to note that basic pH conditions (7–9) are first required to promote the stabilization of disodium terephthalate (NaTA). After LED NIR illumination at different time intervals, the mixture solution was centrifuged to remove the catalyst nanoparticles. The fluorescence emission spectrum of the generated 2-hydroxy disodium terephtalate in the supernatant was subsequently measured at an excitation wavelength of 315 nm.

2.6. Characterization techniques

Fluorescence measurements were performed using a LS55 Fluorescence Spectrometer (PerkinElmer) equipped with a xenon arc lamp as the light source and a quartz cell (10 × 10 mm). Absorption and emission spectra of the CNDs suspensions were systematically acquired at different excitation wavelengths in a UV–vis-NIR spectrophotometer (V-67, Jasco Company) with a quartz cell of 1 cm light path. The pH values were measured with GLP22 (CRISON).

The particle morphology and size distribution were examined by transmission electron microscopy (TEM) (FEI Tecnai T20, operated at 200 kV). The energy-filtered transmission electron microscopy (EFTEM) and high-resolution TEM imaging were done in a FEI Tecnai F30 (operated at 300 kV and equipped with a Gatan Image Filter (GIF Tridiem 863)). Electron energy loss spectroscopy (EELS) measurements were performed on probe-corrected scanning TEM (STEM) FEI Titan Low-Base 60–300 operating at 80 KeV (fitted with a X-FEG® gun and Cs-probe corrector (CESCOR from CEOS GmbH)). EEL spectra were recorded using the spectrum-imaging (SPIM) mode [50–52] in a Gatan GIF Tridiem ESR 865 spectrometer. The energy resolution was ~1.1 eV. The functionalization of the CNDs surface was followed by Fourier transform infrared (FTIR) spectroscopy using a Bruker Vertex 70 FTIR spectrometer.

The surface composition of the samples was analyzed by x-ray photoelectron spectroscopy (XPS) with an Axis Ultra DLD (Kratos Tech.). The spectra were excited by a monochromatic Al Kα source (1486.6 eV) run at 12 kV and 10 mA and pass energy of 20 eV was used. The binding energies were referenced to the internal C 1s (284.3 eV) standard. Analyses of the peaks were performed with CasaXPS software, using a weighted sum of Lorentzian and Gaussian component curves after Shirley background subtraction. Raman analysis was carried out with the aid of a Laser Raman
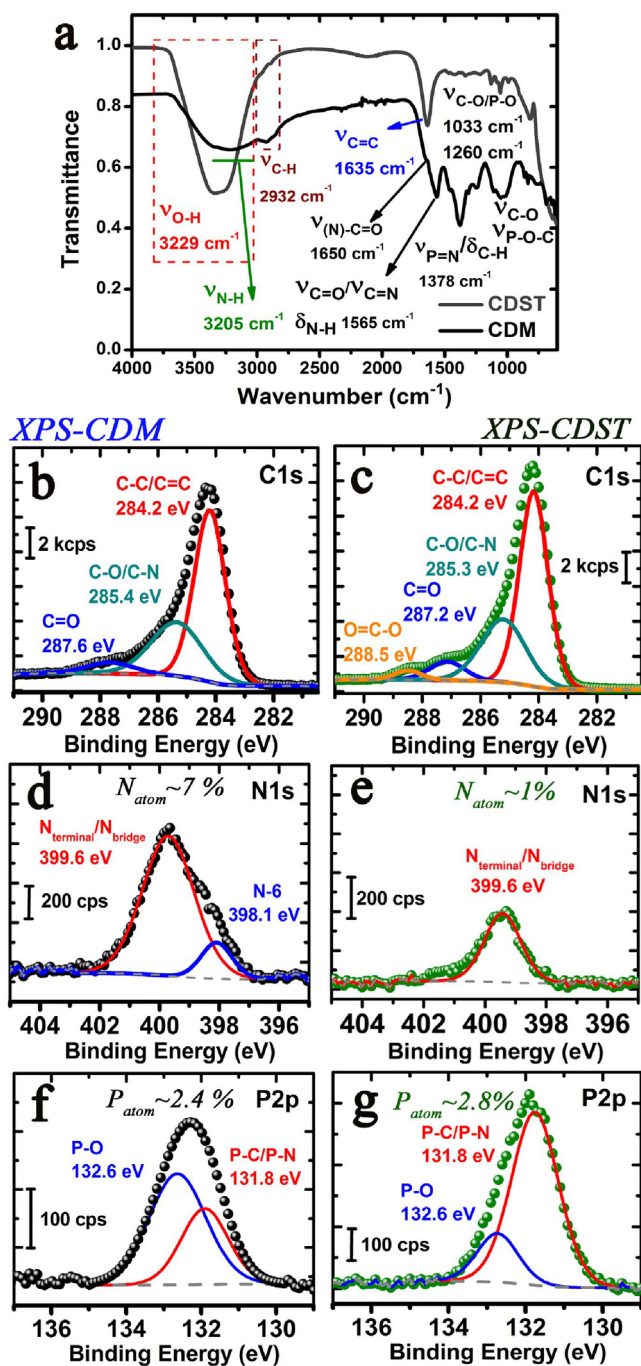
lated to be 9.4% and 15.2%, respectively. To minimize re-absorption effects, the absorbance values of the two solutions in 10 mm cuvettes were kept under 0.1 at the excitation wavelength. Excitation and emission slit widths were set at 7.5 nm when recording PL spectra. Elemental analysis rendered similar compositions for both raw carbogenic sources (Mate herb (%) C:H:N:O:P = 48:5:3:38:5 and Stevia plant (%) C:H:N:O:P = 46:6:3:34:5). The GC–MS instrument (GC–MS Shimadzu QP-2010SE) used for the analysis of reaction intermediates was equipped with a Zebron capillary GC column (30 m x 250 μm, 0.25 μm). A NIST/EPA/NIH mass spectral library (NIST14) was used for identification of *m/z* values. Helium (purity >99.999%) was used as a carrier gas with a flow rate of 1.0 mL min⁻¹, and a 1 μL sample was injected at a split mode. According to previous reports, the temperature of injection was set to 300 °C [53,54]. The column temperature was first kept at 60 °C for 2 min, and raised up to a final temperature of 280 °C at a rate of 10 °C min⁻¹. The detector was a quadrupole mass spectrometer and the temperatures of the ion source and interface were both kept at 250 °C.

2.7. Kinetics of the photodegradation experiments

The kinetics of photocatalytic degradation of 2,4-DCP were adjusted to a Langmuir–Hinshelwood model:

$$r = -\frac{dC}{dt} = \frac{kKC}{1 + KC}$$

where *r* represents the initial rate of photooxidation, *C* the concentration of the reactant, *t* the irradiation time, *k* the rate constant of the reaction and *K* is the adsorption coefficient of the reactant. At micromolar concentrations $C \ll 1$, the equation can be simplified to the apparent first rate order equation:

$$\frac{\ln C_0}{C} = kKt = K_{app}t$$

$$C_t = C_0\, e^{-K_{app}t}$$

where K_{app} is the apparent first order rate constant given by the slope of the graph of ln *C* versus *t* and intercept C_0 is the initial concentration of the organic pollutant.

3. Results and discussion

3.1. Synthesis and characterization of green N, P-codoped carbon nanodots from natural plant leaves

Dried leaves from Mate and Stevia plants were calcined at 300 °C and 250 °C, respectively (Fig. 1a). After purification (see experimental section for details), stable colloidal suspensions of well-dispersed carbon nanoparticles were obtained. Fig. 1b–c show representative TEM images corresponding to the carbon nanodots rendered from Mate (hereafter labeled as CDM) and Stevia (hereafter denoted as CDST). From TEM images, their average diameters were statistically (N > 100 NPs) estimated as 3.0 ± 1.1 nm and 2.5 ± 0.7 nm respectively (Fig. 1d–e). Both samples exhibit a graphitic crystalline structure as shown in the HRTEM images of individual CNDs (see insets in Fig. 1b–c).

The surface chemistry analysis of the CNDs was carried out by FT-IR and XPS. Fig. 2a shows the FT-IR spectra of the CNDs. The CDST shows absorption contributions at ~3230 cm⁻¹ and 1635 cm⁻¹ corresponding to characteristic stretching vibration modes of ν (O—H) and ν (C=C), respectively[55]. Some additional contributions at ~1030–1100 cm⁻¹ were also detected and tentatively attributed to C—O/P-O stretching modes[56–58]. Remarkably, the CDM sample shows additional features at ~3205 cm⁻¹, ~2930 cm⁻¹ that correspond to the stretching bands of ν (N—H) and ν (C—H). Other contributions at ~ 1650 cm⁻¹, ~ 1565 cm⁻¹, ~ 1380 cm⁻¹ and in the

Fig. 2. Surface chemistry analysis of the CNDs: a) FT-IR spectra corresponding to the CDST and the CDM samples, respectively; b)-c) Fitted X-ray photoemission spectra in the C1s region of the CDM and CDST samples, respectively; d)-e) Fitted X-ray photoemission spectra in the N1s region of the CDM and CDST samples, respectively; f)-g) Fitted X-ray photoemission spectra in the P2p region of the CDM and CDST samples, respectively.

WiTec-Alpha 300 spectrometer using an Ar⁺ ion laser exciting at 532 nm. The Raman light was collected in a backscattering geometry. The instrument was calibrated against the Stokes Raman signal of pure Si at 520 cm⁻¹ using a silicon wafer crystal plane surface.

The quantum yield (QY) value of CNDs was calculated by comparing the integrated PL intensities (excited at 360 nm) and absorbance values of CNDs at ~340–345 nm with those of quinine sulphate. Quinine sulphate (QY = 0.54 at 360 nm) was dissolved in 0.1 M H₂SO₄ (refractive index, 1.33) and CNDs were dissolved in water (refractive index, 1.33). QYs of CDM and CDST were calcu-
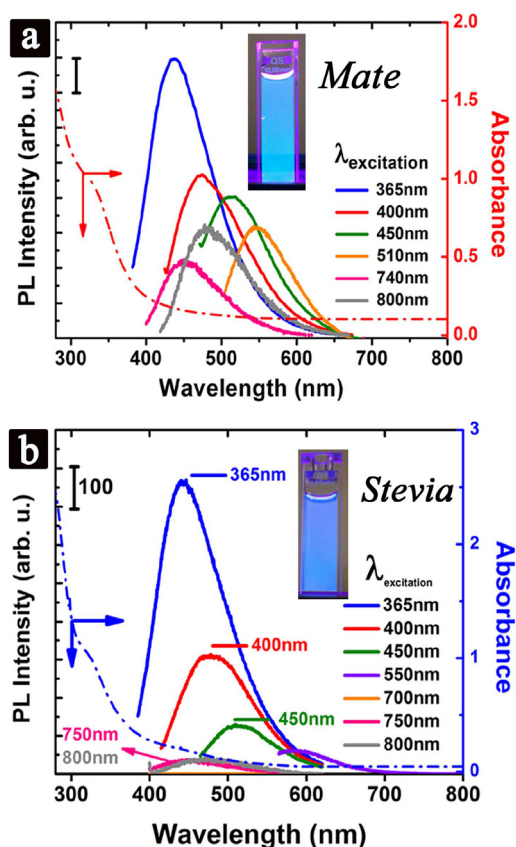
Fig. 3. Optical properties of the CNDs: a) UV–vis absorbance and photoluminescence spectra of the CNDs derived from mate at different excitation wavelengths from 365 to 800 nm; b) UV-vis absorbance and photoluminescence spectra of the CNDs derived from stevia at different excitation wavelengths from 365 to 800 nm; The insets show images of the suspension of the corresponding CNDs under UV light illumination (λ_{exc} = 365 nm). (For interpretation of the references to colour in this figure legend, the reader is referred to the web version of this article.)

centered at ~1350 cm^{-1} and ~1580 cm^{-1} with certain overlapping between them that are typically denoted as D band (typical of structural disorder and defects and sp^3 coordination) and G band (typical of graphitic order and sp^2 bonding), respectively (see Fig. S1). Therefore, both CNDs exhibit a slightly higher contribution from the disordered fraction in agreement with the XPS results (see Fig. 2). It is also noteworthy that both samples seem to show a third contribution located at ~1505 cm^{-1} which has been previously denoted as Dí band and associated with amorphous sp^2-bonded forms of carbon or interstitial defects, thereby pointing out to the existence of outer defective layers in the carbon nanodots [34,65].

Regarding the optical properties of the carbon dots, Fig. 3 displays the UV–vis absorption spectra and the wavelength-dependent photoluminescence (PL) response for both CNDs. These CNDs exhibit a dual behavior as down-converters upon excitation within the 365–510 nm intervals [35] and a more striking up-converting response under NIR irradiation at 750–800 nm [40,41]. The former behavior is traditionally observed in semiconductor-type quantum dots and it is associated with the lower capacity to repopulate the excited states upon excitation with lower energy wavelengths [40,41,43,66,67]. In the particular case of CNDs, the PL emissions in the blue-green range have been attributed to the presence of isolated sp^2 clusters within more extended sp^3 networks [34,68], as suggested from the Raman analysis (Fig. S1).

The up-conversion phenomenon is remarkable for the CNDs derived from mate (Fig. 3a) that display a much stronger PL response in comparison with the stevia counterpart after NIR excitation and a much broader absorption band throughout the whole UV–vis-NIR window (Fig. 3b). Despite continuous efforts to explain this particular behavior, the exact mechanisms behind up-conversion for CNDs have not been unveiled yet. Nevertheless, there is consensus about the influence of doping heteroatoms (i.e. N, S, B, P) [13,68,69] that promote the generation of virtual dopant states close to the LUMO levels of the CNDs thereby enabling longer wavelength multi-photon absorption events and subsequent emissions of single photons at shorter wavelengths during the recombination decay [27,41] (Fig. 3a). Therefore, it seems reasonable to correlate the presence of P and especially N co-dopants in the CDM structure to the broader absorption in the visible range and the enhanced up-converting response in comparison with the CDST sample where the presence of N is rather limited and absorption tail decays at shorter wavelengths than the CDM one (Figs. 2 and 3).

3.2. Synthesis and characterization of CNDs/TiO$_2$ hybrids

Once the optical properties of the CNDs had been established, the next goal was to achieve a successful assembly of both types of CNDs with of the shelf commercial anatase supports to explore their potential capabilities as sensitizers to expand the photocatalytic response beyond the UV range. To do so, both CNDs and TiO$_2$ nanoparticles with anatase phase (Fig. S2) were thoroughly mixed under vigorous stirring for 30 min and then dried under vacuum at 65 °C during 90 min (see Experimental Section). The successful coupling of the CNDs and the TiO$_2$ NPs was confirmed by different TEM analysis approaches. Fig. 4(a) and (c) correspond to low-magnification TEM images of the CNDST decorating the anatase support. Fig. 4(b) and (g) show HRTEM images that clearly corroborate the presence of both CDST and CDM onto the titania particle, respectively. In order to confirm the presence of such nanostructures on the anatase support, an analysis combining high-angle annular dark field (HAADF)-STEM imaging and EDX was performed over the CDM@TiO$_2$ hybrid. The EDX analysis on different regions where CNDs clearly spotted rendered a higher fraction of C signal in comparison with closer areas where CNDs were not apparently deposited (see Fig. 4(e)–(f)).
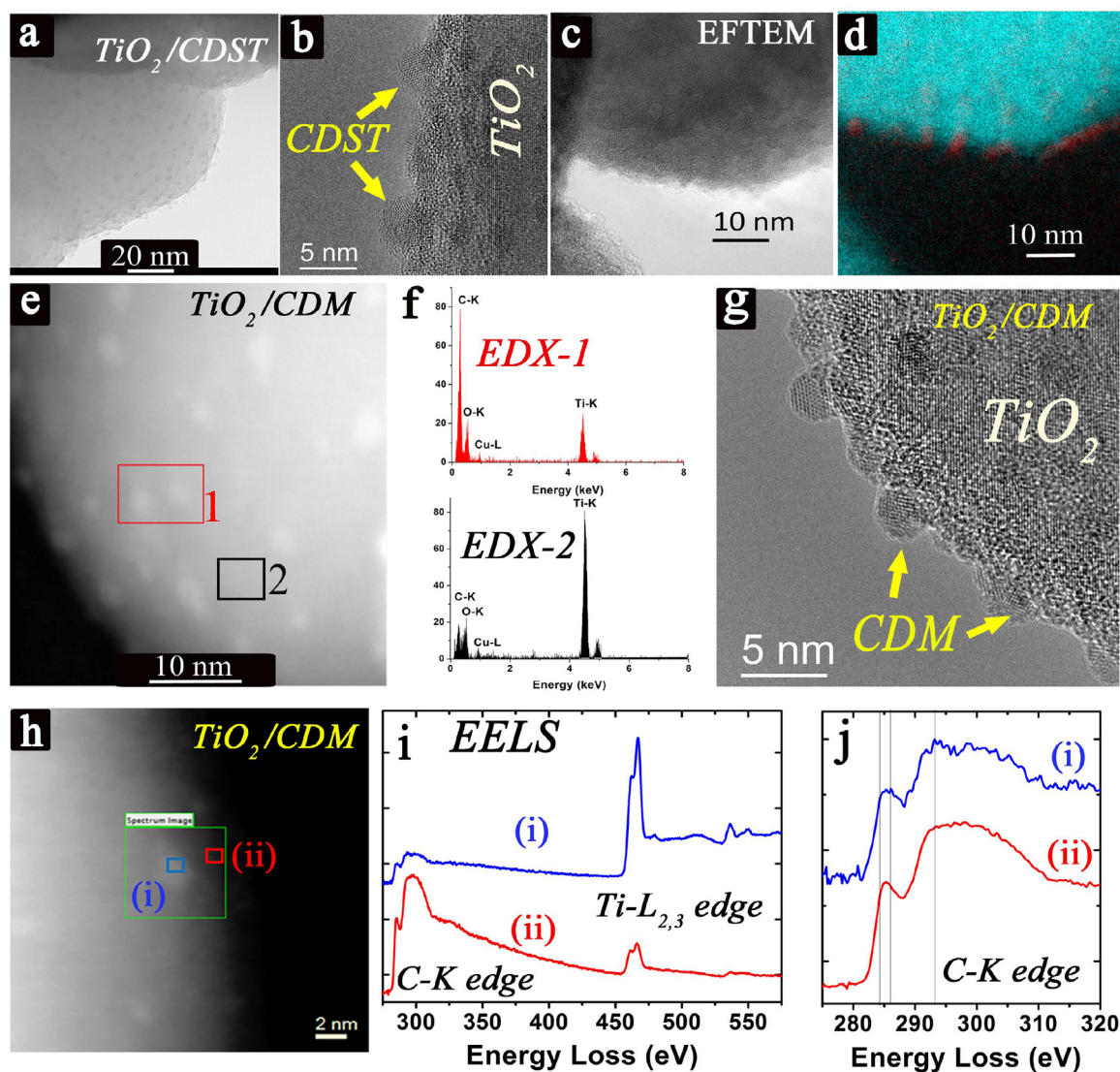
1100–1260 cm^{-1} range (Fig. 2a) have been tentatively identified as C=O, C=N, P=N stretching modes corresponding to aromatic amides and aromatic rings containing P groups, thereby accounting for the partial substitution of C atoms by co-doping elements such as N or P [55–58].

XPS results further corroborate the presence of multiple oxidized carbon moieties on the surface of the CNDs such as O–C=O, C=O, C–O/C–N bonds in the C1s region (Fig. 2b–c). The presence of C–C/C=C bonds is predominant (Fig. 2b–c) although the specific contribution of each specific sp^2 or sp^3 bonding types can not be clearly discerned by this technique [34,59–61]. The presence of nitrogen (see Fig. 2d–g), is especially remarkable for the Mate derived carbon dots, accounting for up to 7% N atomic composition in contrast with the CDST that barely reaches 1% N atoms. The main contribution observed at ca. 399.6 eV in the N1s spectra can be an attributed to N–C bonds in terminal or bridged positions within a carbon network according to Pels and Sanchez-Lopez [33,62–64], although it has also been tentatively associated to amides [64]. It is also worth mentioning that both CNDs present an analogous phosphor atomic composition of ~2.5% P (Fig. 2f–g) with a higher fraction of oxidized P-O species at 132.6 eV in the CDM sample and a higher contribution of P-C/P-N bonds centered at lower BEs (131.8 eV) in the CDST counterpart.

In addition, Raman spectroscopy can be also used as a surface characterization tool of partially ordered carbon materials. The first-order Raman spectra corresponding to both carbon dots samples reveal a similar pattern with two relatively broad bands

Fig. 4. (a) and (c) Low-magnification TEM micrographs of CDST supported on TiO$_2$ nanoparticles; (b) and (g) HRTEM images of the CNDs-TiO$_2$ hybrids including CDST and CDM, respectively; (d) Energy filtered TEM image formed by the superposition of signals stemming from the C-K (in red) and Ti-L$_{2,3}$ edges (in blue and green), respectively. These EFTEM analyses have been performed in the area displayed in the TEM of (c), where the CDST are observed;(e) HAADF-STEM image of the CDM-TiO$_2$ hybrid including marked areas for EDX analysis; (f) EDX spectra corresponding to the areas analyzed in e; (h) HAADF-STEM image of the CDM-TiO$_2$ hybrid including marked areas for EELS analysis; (i) EEL spectra extracted from the SPIM recorded in the area marked in the HAADF image displayed in h. C-K, Ti-L$_{2,3}$ and O-K edges are observe;. (j) Zoom of the C-K edge for the two EEL spectra of Fig. 4 (i), see the text. (For interpretation of the references to colour in this figure legend, the reader is referred to the web version of this article.)

In addition, we performed local chemical TEM analyses via energy-filtered transmission electron microscopy imaging-spectrum (EFTEM) and spatially-resolved electron energy-loss spectroscopy (SR-EELS), see Fig. 4(d) and (i)–(j), respectively. From the EFTEM RGB micrograph (Fig. 4(d)), the presence of C nanostructures (C-K map in red) on the top of the TiO$_2$ particles (Ti-L$_{2,3}$ map in blue and green). This result confirms the presence and the composition of CDSTs spotted by regular TEM in Fig. 4(a)–(c). Analogous results were achieved in the case of CDMs. Furthermore, the hybrids have been analyzed by SR-EELS, which is another very powerful technique to investigate such nanomaterials at sub-nanometer scale [70]. Fig. 4(i) displays two EEL spectra. Each of these two EEL spectra corresponds to the sum of 4 spectra (2 × 2 probe positions of the spectrum-image (SPIM)) recorded in the areas marked on the high-angle annular dark field (HAADF)–STEM image of Fig. 4(h). This HAADF micrograph also shows the position where the SPIM has been acquired. The C-K, Ti-L$_{2,3}$ and O-K edges are visible, and

these signals correspond to the hybrid nanomaterials (carbonnanodots, other form of C materials and TiO$_2$ support NPs).

The Fig. 4(j) shows the energy loss near-edge features (ELNES) of the C-K edge for these two EEL spectra. These ELNES signals consist of a π* peak at ∼285 eV and a well-defined σ* band starting at ∼292 eV [51,52,70–72]. These fingerprints are typical for the sp^2 hybridization of the C atoms. However, we can distinguish the signatures of two different types of C materials. The spectrum displayed in Fig. 4(j-ii) corresponds to an amorphous-like C, likely from some adventitious carbon contamination inherent to the TiO$_2$ nanoparticle. However, the EEL spectrum displayed in Fig. 4(j-i) is closer to the signature of more organized/better structured sp^{2}C nanomaterial. In addition, this EEL spectrum displays two other signatures: a peak at ∼288 eV and another at ∼291.8 eV. These peaks can be assigned to: C=C π* (from CH$_2$ groups, after reduction by the electron beam), and σ* contribution from a carbonyl-like group [71,72].
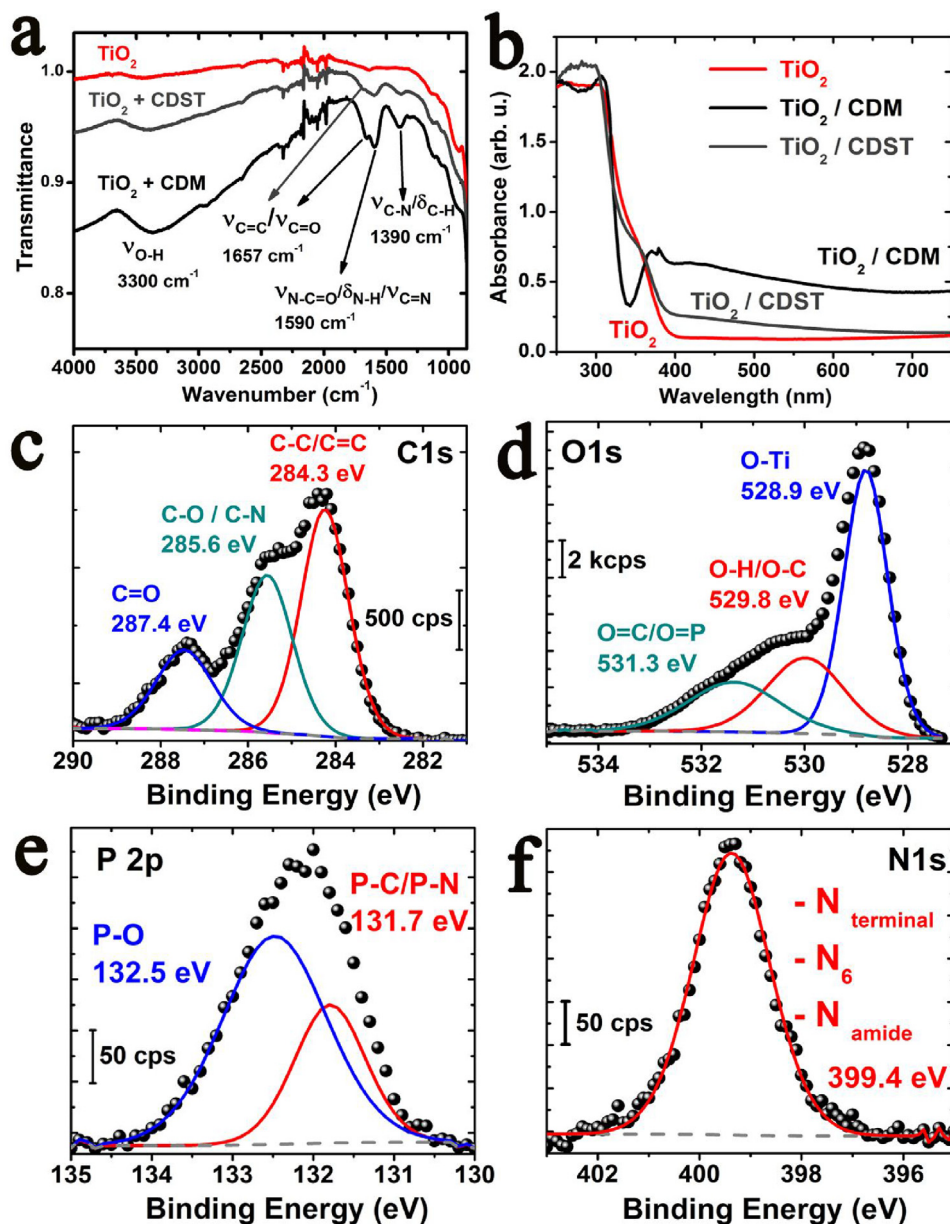
Fig. 5. Surface chemistry analysis of the CND@TiO₂ nanohybrids: a) FT-IR spectra comparing the commercial TiO₂ nanoparticles before and after assembly with CDST and CDM, respectively; b) UV–vis absorption spectra of the TiO₂ anatase nanoparticles before and after the assembly with the CDST and the CDM samples, respectively; Fitted X-ray photoemission spectra of the CDM@TiO₂ hybrid corresponding to: c) the C1s region; d) the O1s region; e) the P2p region and f) the N1s region. Analogous XPS analyses can be found in the Electronic Supplementary Information for the CDST@TiO₂ sample.

FT-IR spectroscopy analysis was also carried out to determine the nature of the interaction between the CNDs and the anatase. The major differences observed with respect to the bare TiO₂ NPs before CNDs assembly are related with the enhanced presence of vibrational bands at 3300 cm⁻¹ attributable to −O−H functional groups as well as the bands at 1657 or 1711 cm⁻¹ that depending on the CNDs, correspond to C=C and/or C=O stretching vibrations[55]. These features further suggest the effective presence of CNDs with their specific surface oxidized states. Furthermore, the broader and red-shifted absorption bands detected below 1250 cm⁻¹ in comparison with the uncoated TiO₂ point out to an effective interaction with the supports through the combination of Ti−O−C and Ti−O−Ti vibrational bands or alternatively to the presence of P−O−C stretching contributions associated to aromatic groups [56–58]. Finally, the additional presence of bands at 1590 and 1390 cm⁻¹ could suggest the presence of amide groups through the presence of stretching

vibrations of N−H and C−N, respectively [55]. These bands look more pronounced on the CDM@TiO₂ hybrids which possess the maximum compositional presence of N species (Fig. 2, Fig. 5a–f). The partial contribution of structural adsorbed water or C−H deformation bands cannot be ruled out [55].

XPS analysis was also performed to study the components and surface chemistry of the CNDs/TiO₂ nanohybrids. At a first glance, a clear increment of the presence of carbon atoms was detected on the surface of the nanohybrids (∼30–32%) in comparison with the bare TiO₂ support (∼19%) suggesting the presence of additional carbonaceous entities (CNDs) accompanying the typical adventitious carbon deposits. Raman analysis of the commercial TiO₂ support (Fig. S3) and the nanocomposites (Fig. S4) further supported the XPS outcome with a small contribution of carbon species in the 1200–1650 cm⁻¹ range in comparison with the strong signal stemming from the anatase phase. The incremental presence of

C—O/C—N bonds at 285.6 eV and especially at 287.4 eV accounting for C=O bonds further corroborates the major presence of surface functional groups associated to the CNDs (Figs. 5c and S5 in SI). Again, the contribution of C—C and especially C=C features is predominant in the C1 s spectrum of both nanocomposites (Figs. 5c and S5) but the specific differentiation can not be properly resolved by this technique [59–61]. The absence of contributions at 281 eV rules out the direct formation of C-Ti bonds and strongly suggests the interaction via C—O—Ti links [30,73,74]. The contributions in the O1s region at 528.9, 529.8 and 531.3 eV are typically ascribed to O-Ti, (H)O—C and O=C/O = P bonds, respectively (Figs. 5d and S5 in SI) and confirm the presence of modified CNDs. Finally, the signal registered from the N1s and P2p regions in the nanohybrids and the absence of an equivalent signal on the original TiO$_2$ support clearly evidences the successful attachment of the CNDs (Figs. 5e–f and S5 in SI). Both CND@TiO$_2$ hybrids rendered an analogous signal in the P2p region accounting for P-O/P-C bonds at 132.5 and 131.7 eV, respectively and a surface atomic percentage slightly superior for the CDST@TiO$_2$ sample (~1.5% vs. ~1% for hybrid containing CDMs). In contrast, the N1 s region rendered a 2.5-fold higher presence of N entities in the CDM@TiO$_2$ hybrid (~2.6% vs. ~0.9%) with a similar contribution centered at 399.4 eV.

Taking into account the formerly described FTIR results (*vide supra*), the N contributions in the mate-derived hybrids can be likely attributed to the combined presence of amides functionalities and aromatic N—C bonds in terminal positions whilst the stevia-derived hybrids only accounts for heteroatomic substitutions in the carbon network [62,64]. Finally, it is worth mentioning that slight shiftings on the binding energies (B.E.) of the Ti2p$_{3/2}$ and Ti2p$_{1/2}$ contributions observed in the photocatalytic CND@TiO$_2$ hybrids are consistent with a stronger interaction between CNDs and TiO$_2$ via C—O—Ti links [30,73,74]. Likewise, the formation of O—Ti—N linkages via N$^-$ anionic species interacting with the TiO$_2$ lattice previously observed in other N-doped CNDs [30,73,74] can be ruled out due to the absence of lower B.E. contributions, even in the CDST@TiO$_2$ samples with lower N content.

From the optical point of view, the effective assembly of the CNDs was also identified by UV–vis spectroscopy in Fig. 5b. A broader absorption band with a tail extending towards the visible-NIR range was detected for both nanohybrids in comparison with the bare support. These changes account for the effective modification of the band gap properties of the semiconductor support and the positive influence of the N, P heteroatoms and different surface state groups able to create novel conjugated and hybridized energy levels (*vide infra* in the next section for further discussion) [56,68,69,75]. It is especially remarkable the enhanced absorption in the CDM@TiO$_2$ composite that can be attributed to the contribution of extra n-π* transitions provided by additional N energy levels [34,76].

3.3. Visible-light driven photodegradation of 2,4-dichlorophenol in the presence of the CNDs@TiO$_2$ nanohybrids

The photocatalytic activity of the CNDs@TiO$_2$ nanohybrids was tested against the degradation of an aqueous solution containing 2,4-DCP, a recalcitrant and toxic pesticide pollutant, under visible light irradiation. Fig. 6a shows the evolution on the concentration of the chlorinated pollutant at different cumulative irradiation times in the visible-light range using a fluorescent lamp with cut-off filter at λ < 420 nm. The photocatalytic response of anatase NPs before and after the assembly with the two CNDs has been compared. It becomes clear that the CNDs positively contribute to enhance the visible-light driven photocatalytic degradation of 2,4-DCP in comparison with the uncoated TiO$_2$ support. After 60 min of irradiation, only the hybrid containing the carbon dots stemming from mate is able to achieve total degradation of 2,4-DCP.
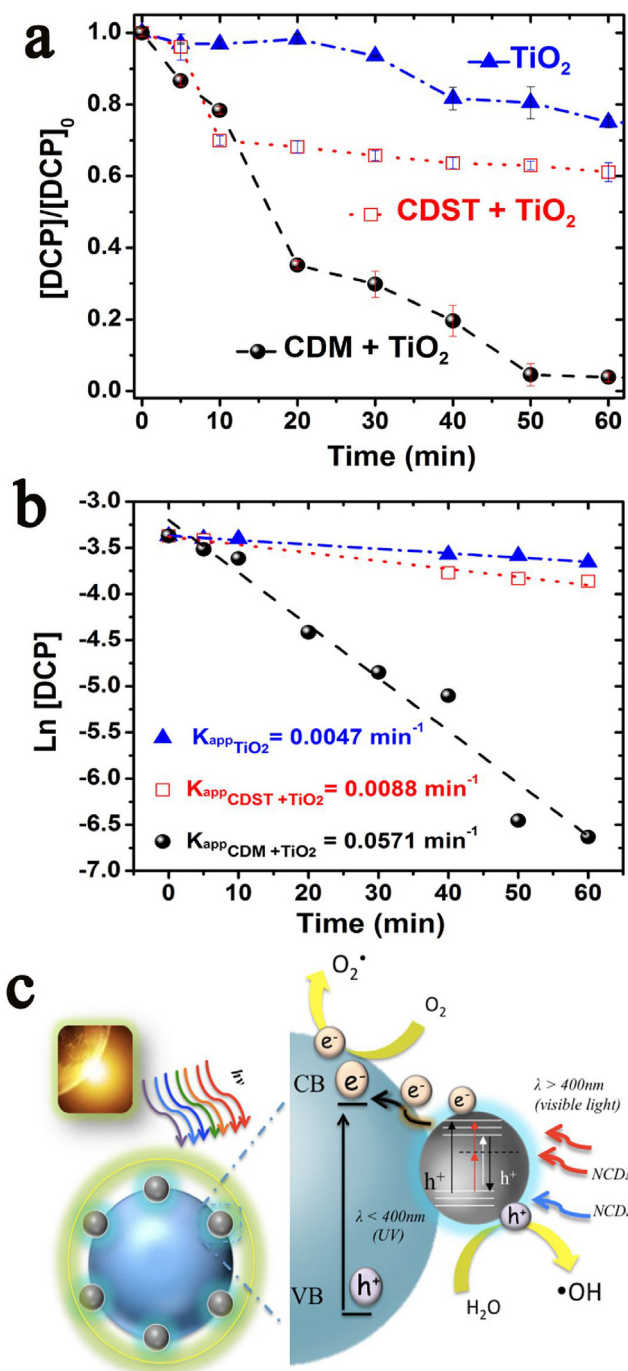

Fig. 6. a) Visible-light driven photocatalytic degradation of 2,4-DCP upon different cumulative irradiation times in the presence of TiO$_2$, CDST@TiO$_2$ and CDM@TiO$_2$, respectively; [2,4-DCP]$_0$ = 0.025 mM; [catalyst] = 0.2 g L^{-1}; b) Apparent kinetic degradation rates (K$_{app}$) for 2,4-DCP obtained from the slope of the semi-log plot for the 2,4-DCP degradation (see Experimental Section for details on the pseudo-first-order kinetic model); c) Schematic view of the most plausible light-induced charge-transfer process occurring on the CNDs@TiO$_2$ nanohybrids.

In contrast, the uncoated TiO$_2$ barely reaches a 30% while the CDST@TiO$_2$ outcome is close to 40% degradation. Therefore, the performance of the CDM@TiO$_2$ clearly exceeds not only that of TiO$_2$, but also the performance of the CDST@TiO$_2$ counterparts accounting for an analogous ~1% wt loading. This is in fact corroborated by the higher apparent rate constants determined for the CDM@TiO$_2$ photocatalyst after the application of a Langmuir-Hinshelwood

Table 1
Summary of recent results related with the visible-light driven photocatalytic degradation of 2,4-dichlorophenol.

Catalyts	Concentration of catalyst or pollutant	Kinetics/Degradation percentages	Irradiation Source	Ref.
$GO/g-C_3N_4$	10 g/L cat 61 mM DCP	$0.008\ min^{-1}$	Xe short arc lamp (CHF-XM35-150W, Beijing Changtuo Co.) served as the visible light source, ($\lambda > 400\ nm$)	[80]
ZnO	0.5 g/L Cat 120 mM DCP	180 min/93%	300 W Xe lamp (PLS-SXE300, Beijing Trusttech Co. Ltd.) equipped with an ultraviolet cutoff filter was employed as the light source to provide visible light ($\lambda \geq 400\ nm$)	[83]
$TiO_2@C$	1 g/L Cat 300 mM DCP	5 h/100%	1000 W halogen lamp was used as the light source of the homemade photoreactor, cooled with flowing water in a quartz cylindrical jacket around the lamp. The short wavelength components were cut-off ($\lambda < 420\ nm$)	[82]
$BiOI@Bi_{12}O_{17}Cl_2$	1 g/L Cat 61 mM DCP	2,4-DCP: 47% in 8 h	visible light irradiation (500 W Xe lamp, $\lambda > 420\ nm$)	[89]
Graphene	0.2 g/L cat 0.123 mM DCP	87% 180 min second-order kinetics	ozone $= 3.188 \times 10^{-3}\ mol/L$	[81]
$Au/\alpha-Bi_2O_3$	1 g/L cat 0.1 mM DCP	65% 7 h	300 W Xe-arc lamp (CHF-XM150, Beijing Trusttech. Co. Ltd.) equipped with a wavelength cutoff filter of $\lambda = 420\ nm$,	[90]
$N-TiO_2$	1 g/L Cat 613 mM DCP	Descomposition rate 55%	A 1000 W halogen lamp was used as the light source of the homemade photoreactor, The short- wavelength components were cut-off ($\lambda < 420\ nm$)	[87]
$Ag-AgI/Al_2O_3$	1.7 g/L Cat 61 mM DCP	81% TOC in 15 min	350 W Xe-arc lamp (Shanghai Photoelectron Device Ltd.) equipped with wavelength cutoff filters for $\lambda > 420$ and 450 nm and focused onto the beaker.	[91]
$N-TiO_2$	1 g/L Cat 613 mM DCP	50%/5 h	1000 W halogen lamp was used as the light source of the homemade photo-reactor, The short wavelength components ($\lambda < 420\ nm$)	[86]
Ag-AgBr/MAP	1.7 g/L Cat 61 mM DCP	100% 20 min	350 W Xe-arc lamp (Shanghai Photoelectron Device Ltd.) equipped with wavelength cutoff filters for $\lambda > 420$ and focused onto the beaker.	[92]
$TiO_2/Au\ NPs$	10 g/L cat	$0.0095\ min^{-1}$ $R^2 = 0.996$	high pressure xenon short arc lamp (CHFXM35−500W, Beijing Changtuo Co.) was served as the light source, a glass filter (ZUL0422, Asahi Spectra Co.) was added to allow visible light ($\lambda > 420\ nm$) to pass through.	[93]
WO_3/TiO_2	1.1 g/L Cat 123 mM DCP	$0.2618\ min^{-1}$	A 1000 W halogen lamp was used as the visible light source (the average light intensity was 60 mW cm−2) and the light from the lamp included beams from ultraviolet and visible light regions. The short-wavelength components ($\lambda < 420\ nm$)	[85]
$\alpha-Fe_2O_3$	1.5 g/L cat 0.5 mM DCP	$1.61E^{-4}\ M/h$	The lamp has a wavelength distribution simulating so- lar radiation showing an integrated photons emission of 7% of the total radiation between 290 and 400 nm. The irradiation vessels used were 60 mL cylindrical Pyrex flasks (cutoff $\lambda \approx$ 290 nm)	[88]
$V-TiO_2$	1 g/L cat 613 mM DCP	8h-90%	300 W high-pressure Hg lamp and a 1000W tungsten halogen lamp equipped with a UV cut-off filters ($\lambda < 420\ nm$)	[84]
Mesoporous- TiO_2	1 g/L cat 0.153 mM DCP	$Kapp = 0.004$	A 1000 W halogen lamp was used as the light source. The short- wavelength components were cut-off ($\lambda < 420\ nm$).	[94]
$RGO/ZnFeO_4/Ag_3PO_4$	2 g/L cat 123 mM DCP	$K = 0.0116\ min^{-1}$ $R^2 = 0.9920$	300 W Xe lamp and a 1000W with a UV cut-off filters ($\lambda < 420\ nm$)	[54]
P25	0.1 g/L cat 1.5 mM DCP	$K = 0.0328\ min^{-1}$	125 W (Philips HPL-N) Hg lamp	[79]
$N-CNDs/TiO_2$	0.2 g/L cat 0.025 mM DCP	90% Degradation 7.5 h	Xe lamp with cutoff filter at $\lambda < 420\ nm$	[30]

model and the adjustment to a pseudo-first-order kinetics (Fig. 6b). The apparent first order constants (k_{app}), determined by linear fitting to the experimental data, indicate a very limited degradation when TiO_2 was used ($k_{app} = 0.0047\ min^{-1}$) that was duplicated upon the assembly of the CDST ($k_{app} = 0.0088\ min^{-1}$) and 10-fold enhanced in the presence of the CDM ($k_{app} = 0.0571\ min^{-1}$) (Fig. 6b). Analogous kinetic constants have been recently reported by Pastrana et al. for nanodiamond-TiO_2 composites deposited by atomic layer deposition toward the decomposition of diphenhydramine, a model pharmaceutical pollutant[69,77]. Likewise, these results have been also compared specifically with other photocatalysts reported for the degradation of 2,4-DCP and summarized in Table 1. Although a great number of studies have been previously devoted to UV-light assisted degradation of phenols [78,79], Table 1 is mainly focused on visible-light driven photocatalytic degradation processes assisted by carbon based systems [80,81], C-decorated titania [30,82], undoped [83] or doped semiconductors [84–87],

iron-based Fenton catalysts [54,88] and plasmonic photocatalysts [89–93]. It is worth mentioning that the CDM@TiO_2 kinetics exhibit an analogous or superior performance, even in comparison with P25 operating in the UV range [79] (k = 0.0328 min^{-1}, see Table 1). Hence, our recent results operating with amine-derived CNDs sensitizers did not achieve total degradation even after longer photoirradiation periods [30].

Some very recent reports have shown the positive influence of combining carbon structures with TiO_2 to improve its visible-light response, including the direct doping of titania with C atoms and the coating with carbonaceous layers, carbon dots or graphene layers [68], largely using model dyes. In contrast, the number of photocatalytic studies devoted to chlorinated wastewater samples or pharmaceutical pollutants has been scarce or more focused on Fenton catalysts and other AOPs [4,68,69,95,96]. Other analogous systems containing carbon-based sensitizing materials in the form of CNDs, Graphene Oxide or C_3N_4 did not outperform our mate-
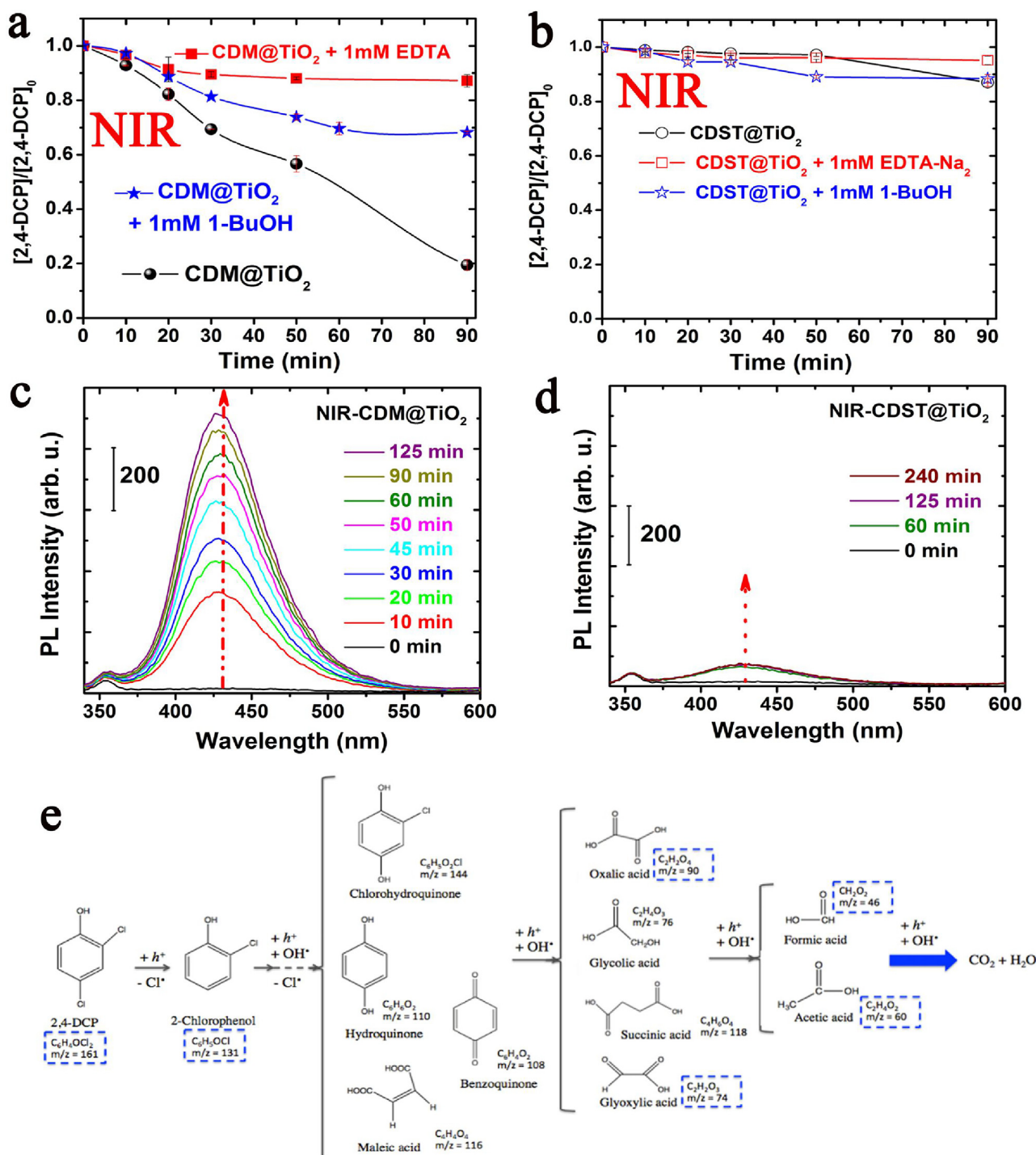
Fig. 7. a) NIR-light driven photocatalytic degradation of 2,4-DCP upon different cumulative irradiation times in the presence of CDM@TiO$_2$ and comparative quenching experiments in the presence of 1-butanol or EDTA-Na$_2$; b) NIR-light driven photocatalytic degradation of 2,4-DCP upon different cumulative irradiation times in the presence of CDST@TiO$_2$ and comparative quenching experiments in the presence of 1-butanol or EDTA-Na$_2$; [2,4-DCP]$_0$ = 0.025 mM; [catalyst] = 0.2 g L^{-1}; c) Fluorescence spectra of the different solutions of the hydroxylated derivative of terephthalic acid after different irradiation times of CDM@TiO$_2$ under NIR-LED light; d) Fluorescence spectra of the different solutions of the hydroxylated derivative of terephthalic acid after different irradiation times of CDST@TiO$_2$ under NIR-LED light; Experimental conditions describe in the Experimental section; e) Proposed reaction and degradation mechanism of 2,4-DCP based on previous results on the literature and the reaction intermediates detected by GC–MS analysis (highlighted with dashed rectangles).

based photocatalytic nanocomposite (see Table 1). Here we not only show that the combination of carbon structures with anatase can be used for the efficient photocatalytic degradation of recalcitrant pollutants (2,4-DCP), but also that these carbon structures must have certain physicochemical properties to be effective, i.e.,

not all carbon dots are alike even when, as in this case, they are of similar size and obtained through analogous routes from natural plants. This accounts for the high charge-transfer efficiency of the CDM in a broader spectral range attributable to their upconversion properties.

The light-induced charge-transfer mechanism likely responsible for the photocatalytic efficiency of the CDM@TiO$_2$ nanohybrid in the visible range, is schematically displayed in Fig. 6c. The presence of N and P heteroatoms in the CNDs favors a broader absorption capacity in the visible range due to the introduction of additional dopant-induced states close to the LUMO level of the CNDs (n → π* transitions caused by C=N, C = P conjugated bonds). Moreover, the presence of surface oxidized groups such as C=O, P = O or COOH can additionally favor band-bending effects and a more effective separation of photocarriers due to the partial hybridation of π levels of carbon and O2p levels located above the HOMO level of the CNDs [68,96]. Therefore, CNDs act as effective photosensitizing agents and electron reservoirs able to improve the charge-transfer photoinduced ability of the anatase NPs by facilitating the mobility of electrons to the conduction band of TiO$_2$ and concomitantly hindering recombination. The electrons can be shuttled freely along the conducting network of CNDs, while the longer-lived holes on TiO$_2$ account for the higher activity of the complex photocatalyst system. The electron/hole pairs then react with the adsorbed oxidants/reducers (usually O$_2$/OH$^-$) to generate reactive oxygen species (e.g. •O$_2^-$, •OH), which cause degradation of the organics contaminant proposed.

In order to corroborate the proposed mechanism and the role of the upconverting CDM, an additional set of photodegradation experiments were carried out upon illumination with a specific NIR-LED operating at 740 nm. In addition, a series of quenching experiments in the presence of 1-butanol and EDTA-Na$_2$ (a hydroxyl and hole scavenger, respectively) [54,97] were also performed to assess the role of these ROS in the overall degradation of 2,4-DCP. Hence, the in-situ and selective generation of ·OH radicals under NIR illumination was also confirmed with the aid of terephthalic acid, a selective probe that becomes fluorescent only when interacts with these hydroxyl radicals [30,49]. Fig. 7a–b shows the clear differences between the photocatalytic performance of the CDM@TiO$_2$ composites and the CDST@TiO$_2$ ones. This result further supports the expanded sensitizing action of the upconverting nanodots even beyond the visible range. It also demonstrates the active role of the OH radicals in the effective photodegradation of the pollutant (Fig. 7c–d). More importantly, it attributes a very active and important role to the presence of holes given the detrimental effect of EDTA-Na$_2$ on the photodegradation effectiveness (Fig. 7a).

A plausible degradation pathway for the 2,4-DCP is proposed and depicted in Fig. 7e. This scheme is based on previous works in the literature [53,54,98,99] and the intermediates detected by GC–MS analysis in our system at different irradiation times. These analyses detected that the 2-Chlorophenol (m/z = 131, exact mass 128) is the aromatic intermediate formed, and its concentration decreases sharply at the beginning the photocatalytic time, giving rise to the appearance of other acidic reaction intermediates of low molecular weight, such as glyoxylic acid (m/z = 74), oxalic acid (m/z = 90), formic acid (m/z = 46), and acetic acid (m/z = 60), suggesting that CNDM@TiO$_2$ system is effective towards the degradation of 2,4-DCP.

Finally, it is also worth mentioning that both CDM@TiO$_2$ and CDST@TiO$_2$ catalysts could be easily recycled by simple centrifugation and replacement of the pollutant solution. The results (Fig. S6 in SI) showed no loss of activity over 4 reuse cycles and the TEM inspection of the reused photocatalysts did not show any relevant morphological modification on the catalysts after multiple reaction cycles (Fig. S7). Interestingly, the stevia based nanocomposites revealed an apparently major fraction of a carbonaceous layer covering the outer surface of the catalyst particles that we attribute as one potential cause for the deactivation observed in their photocatalytic activity (Fig. 6a) as a result of the formation and/or co-deposition of a competing reaction intermediate that modified the degradation kinetics of the 2,4-DCP [100,101].

4. Conclusions

Upconverting carbon nanodots prepared by pyrolysis of Mate herb leaves have shown excellent response as photosensitizers to expand the photocatalytic activity of anatase supports into the visible range. Interestingly, carbon nanodots with a similar or smaller size prepared from Stevia plant leaves using the same process did not show upconverting properties and displayed a considerably smaller photocatalytic activity (though they were still more active than commercial anatase or P25 under visible light). Both types of CND/TiO$_2$ hybrids show similar presence of oxygenated species on their surface, and analogous content of P. The main difference in the physicochemical characterization is the higher content of N-containing species on the CDM@TiO$_2$. This higher presence of N heteroatoms seems to be determinant on the broader absorption capabilities of the CDM spanning from visible to NIR and their enhanced up-converting behavior. Thus, the much higher photocatalytic activity of this nanohybrid can be explained as the result of the capacity of the CDM@TiO$_2$ to absorb light in a broader range (including NIR) and inject electrons in the conduction band of anatase to generate highly reactive holes and hydroxyl radicals.

Appendix A. Supplementary data

Supplementary data associated with this article can be found, in the online version, at **http://dx.doi.org/10.1016/j.apcatb.2017.06.021**.

References

[1] C.C. Wang, J.R. Li, X.L. Lv, Y.Q. Zhang, G.S. Guo, Energy Environ. Sci. 7 (2014) 2831–2867.
[2] M.C. Ortega-Liebana, E. Sanchez-Lopez, J. Hidalgo-Carrillo, A. Marinas, J.M. Marinas, F.J. Urbano, Appl. Catal. B Environ. 127 (2012) 316–322.
[3] M. Pelaez, N.T. Nolan, S.C. Pillai, M.K. Seery, P. Falaras, A.G. Kontos, P.S.M. Dunlop, J.W.J. Hamilton, J.A. Byrne, K. O'Shea, M.H. Entezari, D.D. Dionysiou, Appl. Catal. B-Environ. 125 (2012) 331–349.

[4] U.I. Gaya, A.H. Abdullah, J. Photochem. Photobiol. C Photochem. Rev. 9 (2008) 1–12.
[5] H. Barndok, M. Pelaez, C. Han, W.E. Platten, P. Campo, D. Hermosilla, A. Blanco, D.D. Dionysiou, Environ. Sci. Pollut. Res. 20 (2013) 3582–3591.
[6] A.O. Ibhadon, P. Fitzpatrick, Catalysts 3 (2013) 189–218.
[7] J.L. Wang, L.J. Xu, Crit. Rev. Environ. Sci. Technol. 42 (2012) 251–325.
[8] A. Kubacka, M. Fernandez-Garcia, G. Colon, Chem. Rev. 112 (2012) 1555–1614.
[9] A.L. Linsebigler, G.Q. Lu, J.T. Yates, Chem. Rev. 95 (1995) 735–758.
[10] A. Dhakshinamoorthy, S. Navalon, A. Corma, H. Garcia, Energy Environ. Sci. 5 (2012) 9217–9233.
[11] E.M. Rodriguez, G. Fernandez, P.M. Alvarez, R. Hernandez, F.J. Beltran, Appl. Catal. B-Environ. 102 (2011) 572–583.
[12] G. Zhang, G. Kim, W. Choi, Energy Environ. Sci. 7 (2014) 954–966.
[13] S. Banerjee, S.C. Pillai, P. Falaras, K.E. O'Shea, J.A. Byrne, D.D. Dionysiou, J. Phys. Chem. Lett. 5 (2014) 2543–2554.
[14] M. Miyauchi, H. Irie, M. Liu, X.Q. Qiu, H.G. Yu, K. Sunada, K. Hashimoto, J. Phys. Chem. Lett. 7 (2016) 75–84.
[15] N. Hintsho, L. Petrik, A. Nechaev, S. Titinchi, P. Ndungu, Appl. Catal. B Environ. 156 (2014) 273–283.
[16] S. Sarina, E.R. Waclawik, H.Y. Zhu, Green Chem. 15 (2013) 1814–1833.
[17] X. Chen, H.Y. Zhu, J.C. Zhao, Z.T. Zheng, X.P. Gao, Angew. Chem. Int. Ed. 47 (2008) 5353–5356.
[18] P.Y. Zhang, T. Song, T.T. Wang, H.P. Zeng, Appl. Catal. B Environ. 206 (2017) 328–335.
[19] J.Y. Qin, H.P. Zeng, Appl. Catal. B Environ. 209 (2017) 161–173.
[20] J.Y. Qin, J.P. Huo, P.Y. Zhang, J. Zeng, T.T. Wang, H.P. Zeng, Nanoscale 8 (2016) 2249–2259.
[21] P.Y. Zhang, T.T. Wang, H.P. Zeng, Appl. Surf. Sci. 391 (2017) 404–414.
[22] T. Ohno, M. Akiyoshi, T. Umebayashi, K. Asai, T. Mitsui, M. Matsumura, Appl. Catal. A Gen. 265 (2004) 115–121.
[23] X.P. Wang, Y.X. Tang, M.Y. Leiw, T.T. Lim, Appl. Catal. A Gen. 409 (2011) 257–266.
[24] Y. Huang, W.K. Ho, Z.H. Ai, X.A. Song, L.Z. Zhang, S.C. Lee, Appl. Catal. B Environ. 89 (2009) 398–405.
[25] G.W. Cui, W.L. Wang, M.Y. Ma, M. Zhang, X.Y. Xia, F.Y. Han, X.F. Shi, Y.Q. Zhao, Y.B. Dong, B. Tang, Chem. Commun. 49 (2013) 6415–6417.
[26] Z.P. Zhang, J. Zhang, N. Chen, L.T. Qu, Energy Environ. Sci. 5 (2012) 8869–8890.
[27] H.T. Li, Z.H. Kang, Y. Liu, S.T. Lee, J. Mater. Chem. 22 (2012) 24230–24253.
[28] A. Tarasov, G. Trusov, A. Minnekhanov, D. Gil, E. Konstantinova, E. Goodilin, Y. Dobrovolsky, J. Mater. Chem. A 2 (2014) 3102–3109.
[29] L. Cao, S. Sahu, P. Anilkumar, C.E. Bunker, J.A. Xu, K.A.S. Fernando, P. Wang, E.A. Guliants, K.N. Tackett, Y.P. Sun, J. Am. Chem. Soc. 133 (2011) 4754–4757.
[30] M.C. Ortega-Liebana, J.L. Hueso, S. Ferdousi, K.L. Yeung, J. Santamaria, Diam. Relat. Mater. 65 (2016) 176–182.
[31] M.C. Ortega-Liebana, J.L. Hueso, A. Larrea, V. Sebastian, J. Santamaria, Chem. Commun. 51 (2015) 16625–16628.
[32] P.C. Hsu, Z.Y. Shih, C.H. Lee, H.T. Chang, Green Chem. 14 (2012) 917–920.
[33] M.C. Ortega-Liebana, M.M. Encabo-Berzosa, M.J. Ruedas-Rama, J.L. Hueso, Chem. Eur. J. 23 (2017) 3067–3073.
[34] M.C. Ortega-Liebana, N.X. Chung, R. Limpens, L. Gomez, J.L. Hueso, J. Santamaria, T. Gregorkiewicz, Carbon 117 (2017) 437–446.
[35] S.N. Baker, G.A. Baker, Angew. Chem. Int. Ed. 49 (2010) 6726–6744.
[36] S.T. Yang, L. Cao, P.G.J. Luo, F.S. Lu, X. Wang, H.F. Wang, M.J. Meziani, Y.F. Liu, G. Qi, Y.P. Sun, J. Am. Chem. Soc. 131 (2009) 11308.
[37] R.L. Liu, D.Q. Wu, S.H. Liu, K. Koynov, W. Knoll, Q. Li, Angew. Chem. Int. Ed. 48 (2009) 4598–4601.
[38] L. Cao, X. Wang, M.J. Meziani, F.S. Lu, H.F. Wang, P.J.G. Luo, Y. Lin, B.A. Harruff, L.M. Veca, D. Murray, S.Y. Xie, Y.P. Sun, J. Am. Chem. Soc. 129 (2007) 11318.
[39] Y.P. Sun, B. Zhou, Y. Lin, W. Wang, K.A.S. Fernando, P. Pathak, M.J. Meziani, B.A. Harruff, X. Wang, H.F. Wang, P.J.G. Luo, H. Yang, M.E. Kose, B.L. Chen, L.M. Veca, S.Y. Xie, J. Am. Chem. Soc. 128 (2006) 7756–7757.
[40] S.J. Zhuo, M.W. Shao, S.T. Lee, ACS Nano 6 (2012) 1059–1064.
[41] Z.X. Gan, X.L. Wu, G.X. Zhou, J.C. Shen, P.K. Chu, Adv. Opt. Mater. 1 (2013) 554–558.
[42] A. Salinas-Castillo, M. Ariza-Avidad, C. Pritz, M. Camprubi-Robles, B. Fernandez, M.J. Ruedas-Rama, A. Megia-Fernandez, A. Lapresta-Fernandez, F. Santoyo-Gonzalez, A. Schrott-Fischer, L.F. Capitan-Vallvey, Chem. Commun. 49 (2013) 1103–1105.
[43] Y. Xu, M. Wu, Y. Liu, X.Z. Feng, X.B. Yin, X.W. He, Y.K. Zhang, Chem. Eur. J. 19 (2013) 2276–2283.
[44] C.F. Wang, X. Wu, X.P. Li, W.T. Wang, L.Z. Wang, M. Gu, Q. Li, J. Mater. Chem. 22 (2012) 15522–15525.
[45] W.L. Ong, M. Gao, G.W. Ho, Nanoscale 5 (2013) 11283–11290.
[46] J. Wang, Y.F. Lim, G.W. Ho, Nanoscale 6 (2014) 9673–9680.
[47] J. Wang, Y.H. Ng, Y.F. Lim, G.W. Ho, RSC Adv. 4 (2014) 44117–44123.
[48] M.J. Krysmann, A. Kelarakis, P. Dallas, E.P. Giannelis, J. Am. Chem. Soc. 134 (2012) 747–750.
[49] M.C. Ortega-Liebana, J.L. Hueso, R. Arenal, J. Santamaria, Nanoscale 9 (2017) 1787–1792.
[50] C. Jeanguillaume, C. Colliex, Ultramicroscopy 28 (1989) 252–257.
[51] R. Arenal, F. de la Pena, O. Stephan, M. Walls, M. Tence, A. Loiseau, C. Colliex, Ultramicroscopy 109 (2008) 32–38.
[52] Francis Leonard Deepak, Alvaro Mayoral, R. Arenal, Advanced Transmission Electron Microscopy: Applications to Nanomaterials, Springer, 2015.
[53] L.J. Xu, J.L. Wang, Appl. Catal. B Environ. 123 (2012) 117–126.
[54] X.J. Chen, Y.Z. Dai, J. Guo, T.H. Liu, X.Y. Wang, Ind. Eng. Chem. Res. 55 (2016) 568–578.
[55] E. Pretsch, P. Bühlmann, C. Affolter, A. Herrera, R. Martinez, Structure Determination of Organic Compounds, Springer, New York, 2000.
[56] C.F. Wang, D. Sun, K.L. Zhuo, H.C. Zhang, J.J. Wang, RSC Adv. 4 (2014) 54060–54065.
[57] X.C. Sun, C. Bruckner, Y. Lei, Nanoscale 7 (2015) 17278–17282.
[58] X.J. Gong, W.J. Lu, Y. Liu, Z.B. Li, S.M. Shuang, C. Dong, M.M.F. Choi, J. Mater. Chem. B 3 (2015) 6813–6819.
[59] H. Fu, Z.J. Du, W. Zou, H.Q. Li, C. Zhang, Carbon 65 (2013) 112–123.
[60] W.J. Peng, H.Q. Li, S.X. Song, ACS Appl. Mater. Interfaces 9 (2017) 5204–5212.
[61] B. Xie, L. Hong, P. Chen, B. Zhu, Bull. Polym. 73 (2016) 891–908.
[62] J.R. Pels, F. Kapteijn, J.A. Moulijn, Q. Zhu, K.M. Thomas, Carbon 33 (1995) 1641–1653.
[63] J.C. Sanchez-Lopez, C. Donnet, F. Lefebvre, C. Fernandez-Ramos, A. Fernandez, J. Appl. Phys. 90 (2001) 675–681.
[64] J.L. Hueso, J.P. Espinos, A. Caballero, J. Cotrino, A.R. Gonzalez-Elipe, Carbon 45 (2007) 89–96.
[65] J.P. Boudou, J.I. Paredes, A. Cuesta, A. Martinez-Alonso, J.M.D. Tascon, Carbon 41 (2003) 41–56.
[66] L. Wang, S.J. Zhu, H.Y. Wang, Y.F. Wang, Y.W. Hao, J.H. Zhang, Q.D. Chen, Y.L. Zhang, W. Han, B. Yang, H.B. Sun, Adv. Opt. Mater. 1 (2013) 264–271.
[67] J.H. Shen, Y.H. Zhu, C. Chen, X.L. Yang, C.Z. Li, Chem. Commun. 47 (2011) 2580–2582.
[68] H.J. Yu, R. Shi, Y.F. Zhao, G.I.N. Waterhouse, L.Z. Wu, C.H. Tung, T.R. Zhang, Adv. Mater. 28 (2016) 9454–9477.
[69] S. Yu, H.J. Yun, Y.H. Kim, J. Yi, Appl. Catal. B Environ. 144 (2014) 893–899.
[70] A.C.Y. Liu, R. Arenal, D.J. Miller, X.D. Chen, J.A. Johnson, O.L. Eryilmaz, A. Erdemir, J.B. Woodford, Phys. Rev. B (2007) 75.
[71] R. Arenal, L. De Matteis, L. Custardoy, A. Mayoral, M. Tence, V. Grazu, J.M. De La Fuente, C. Marquina, M.R. Ibarra, ACS Nano 7 (2013) 4006–4013.
[72] R. Arenal, K. March, C.P. Ewels, X. Rocquefelte, M. Kociak, A. Loiseau, O. Stephan, Nano Lett. 14 (2014) 5509–5516.
[73] A.P. Bhirud, S.D. Sathaye, R.P. Waichal, J.D. Ambekar, C.J. Park, B.B. Kale, Nanoscale 7 (2015) 5023–5034.
[74] M. Sathish, B. Viswanathan, R.P. Viswanath, C.S. Gopinath, Chem. Mater. 17 (2005) 6349–6353.
[75] X.J. Yu, J.J. Liu, Y.C. Yu, S.L. Zuo, B.S. Li, Carbon 68 (2014) 718–724.
[76] Y.Q. Dong, H.C. Pang, H.B. Yang, C.X. Guo, J.W. Shao, Y.W. Chi, C.M. Li, T. Yu, Angew. Chem. Int. Ed. 52 (2013) 7800–7804.
[77] L.M. Pastrana-Martinez, S. Morales-Torres, S.A.C. Carabineiro, J.G. Buijnsters, J.L. Faria, J.L. Figueiredo, A.M.T. Silva, ChemPlusChem 78 (2013) 801–807.
[78] M. Pera-Titus, V. Garcia-Molina, M.A. Banos, J. Gimenez, S. Esplugas, Appl. Catal. B Environ. 47 (2004) 219–256.
[79] W.F. Jardim, S.G. Moraes, M.M.K. Takiyama, Water Res. 31 (1997) 1728–1732.
[80] G.Z. Liao, S. Chen, X. Quan, H.T. Yu, H.M. Zhao, J. Mater. Chem. 22 (2012) 2721–2726.
[81] H.Q. Sun, S.Z. Liu, G.L. Zhou, H.M. Ang, M.O. Tade, S.B. Wang, ACS Appl. Mater. Interfaces 4 (2012) 5466–5471.
[82] J. Zhong, F. Chen, J.L. Zhang, J. Phys. Chem. C 114 (2010) 933–939.
[83] J.P. Wang, Z.Y. Wang, B.B. Huang, Y.D. Ma, Y.Y. Liu, X.Y. Qin, X.Y. Zhang, Y. Dai, ACS Appl. Mater. Interfaces 4 (2012) 4024–4030.
[84] B.Z. Tian, C.Z. Li, F. Gu, H.B. Jiang, Y.J. Hu, J.L. Zhang, Chem. Eng. J. 151 (2009) 220–227.
[85] S.A.K. Leghari, S. Sajjad, F. Chen, J.L. Zhang, Chem. Eng. J. 166 (2011) 906–915.
[86] M.Y. Xing, J.L. Zhang, F. Chen, Appl. Catal. B Environ. 89 (2009) 563–569.
[87] Y. Cong, J.L. Zhang, F. Chen, M. Anpo, J. Phys. Chem. C 111 (2007) 6976–6982.
[88] J. Bandara, J.A. Mielczarski, A. Lopez, J. Kiwi, Appl. Catal. B Environ. 34 (2001) 321–333.
[89] H.W. Huang, K. Xiao, Y. He, T.R. Zhang, F. Dong, X. Du, Y.H. Zhang, Appl. Catal. B Environ. 99 (2016) 75–86.
[90] H.Y. Jiang, K. Cheng, J. Lin, Phys. Chem. Chem. Phys. 14 (2012) 12114–12121.
[91] C. Hu, T.W. Peng, X.X. Hu, Y.L. Nie, X.F. Zhou, J.H. Qu, H. He, J. Am. Chem. Soc. 132 (2010) 857–862.
[92] X.F. Zhou, C. Hu, X.X. Hu, T.W. Peng, J.H. Qu, J. Phys. Chem. C 114 (2010) 2746–2750.
[93] Y. Lu, H.T. Yu, S. Chen, X. Quan, H.M. Zhao, Environ. Sci. Technol. 46 (2012) 1724–1730.
[94] S. Shamaila, A.K.L. Sajjad, F. Chen, J.L. Zhang, Appl. Catal. B Environ. 94 (2010) 272–280.
[95] M.J. Sampaio, L.M. Pastrana-Martinez, A.M.T. Silva, J.G. Buijnsters, C. Han, C.G. Silva, S.A.C. Carabineiro, D.D. Dionysiou, J.L. Faria, RSC Adv. 5 (2015) 58363–58370.
[96] T.F. Yeh, C.Y. Teng, S.J. Chen, H.S. Teng, Adv. Mater. 26 (2014) 3297.
[97] H. Chen, Z.L. Zhang, Z.L. Yang, Q. Yang, B. Li, Z.Y. Bai, Chem. Eng. J. 273 (2015) 481–489.
[98] S.P. Li, X.L. Ma, L.J. Liu, X.H. Cao, RSC Adv. 5 (2015) 1902–1909.
[99] Q. Huang, M.H. Cao, Z.H. Ai, L.Z. Zhang, Appl. Catal. B Environ. 162 (2015) 319–326.
[100] P. Fernandez-Ibanez, M.I. Polo-Lopez, S. Malato, S. Wadhwa, J.W.J. Hamilton, P.S.M. Dunlop, R. D'Sa, E. Magee, K. O'Shea, D.D. Dionysiou, J.A. Byrne, Chem. Eng. J. 261 (2015) 36–44.
[101] M. Romero, J. Blanco, B. Sanchez, A. Vidal, S. Malato, A.I. Cardona, E. Garcia, Sol. Energy 66 (1999) 169–182.